On the Development of Above-Anvil Cirrus Plumes in Extratropical Convection

CAMERON R. HOMEYER

School of Meteorology, University of Oklahoma, Norman, Oklahoma

JOEL D. MCAULIFFE

Department of Geography, Planning, and Environment, East Carolina University, Greenville, North Carolina

KRISTOPHER M. BEDKA

NASA Langley Research Center, Hampton, Virginia

(Manuscript received 22 September 2016, in final form 14 February 2017)

ABSTRACT

Expansive cirrus clouds present above the anvils of extratropical convection have been observed in satellite and aircraft-based imagery for several decades. Despite knowledge of their occurrence, the precise mechanisms and atmospheric conditions leading to their formation and maintenance are not entirely known. Here, the formation of these cirrus ''plumes'' is examined using a combination of satellite imagery, four-dimensional ground-based radar observations, assimilated atmospheric states from a state-of-the-art reanalysis, and idealized numerical simulations with explicitly resolved convection. Using data from 20 recent events (2013–present), it is found that convective cores of storms with above-anvil cirrus plumes reach altitudes 1–6 km above the tropopause. Thus, it is likely that these clouds represent the injection of cloud material into the lower stratosphere. Comparison of storms with above-anvil cirrus plumes and observed tropopause-penetrating convection without plumes reveals an association with large vector differences between the motion of a storm and the environmental wind in the upper troposphere and lower stratosphere (UTLS), suggesting that gravity wave breaking and/or stretching of the tropopause-penetrating cloud are/is more prevalent in plume-producing storms. A weak relationship is found between plume occurrence and the stability of the lower stratosphere (or tropopause structure), and no relationship is found with the duration of stratospheric penetration or stratospheric humidity. Idealized model simulations of tropopause-penetrating convection with small and large magnitudes of storm-relative wind in the UTLS are found to reproduce the observationally established storm-relative wind relationship and show that frequent gravity wave breaking is the primary mechanism responsible for plume formation.

1. Introduction

Aircraft, satellite imagery, and modern satellite-based radar and lidar systems have revealed the presence of cirrus clouds above the anvils of deep extratropical convection for several decades (e.g., Fujita 1982; Adler et al. 1983; Mack et al. 1983; Spinhirne et al. 1983; Setvák and Doswell 1991; Levizzani and Setvák 1996; Wang 2003; Setvák et al. 2013; Bedka et al. 2015). While often not the primary focus of previous studies, they have been suggested to represent the injection of cloud particles into the lower stratosphere and have been associated with severe weather at Earth's surface. However, these linkages and the formation, maintenance, and additional characteristics of above-anvil cirrus are not entirely understood.

Linkages between stratospheric injection of cloud particles and above-anvil cirrus have primarily been based on the fact that they are often warmer in infrared satellite imagery than the surrounding anvil, which is argued to be evidence of their mixing into and thermal adjustment to the typically warmer lower stratosphere.

Supplemental information related to this paper is available at the Journals Online website: http://dx.doi.org/10.1175/JAS-D-16-0269.s1.

Corresponding author e-mail: Cameron R. Homeyer, chomeyer@ou.edu

DOI: 10.1175/JAS-D-16-0269.1

As such, above-anvil cirrus have been associated with the well-known enhanced-V infrared cloud-top feature that has been linked with severe weather at Earth's surface (e.g., Adler et al. 1981; Fujita 1982; Negri 1982; Mack et al. 1983; McCann 1983; Adler et al. 1985; Brunner et al. 2007; Homeyer 2014). Additional justification for the stratospheric injection hypothesis is the association of above-anvil cirrus with overshooting tops (cloud protrusions above anvil clouds sourced by strong convective updrafts, which often represent convective penetration of the tropopause). In particular, when identified in satellite imagery, above-anvil cirrus are typically extensive, stretching from the location of an overshooting top to near the edge of the downstream anvil and resembling a chimney plume. As a result, these extensive above-anvil cirrus clouds are typically referred to as "plumes."

Modeling studies add further credence to the stratospheric injection argument and often suggest that gravity wave generation and subsequent breaking near the overshooting top is a necessary condition for above-anvil cirrus formation (e.g., Wang 2003; Wang et al. 2016). Lofting of cloud material during a wave breaking event is consistent with the early physical descriptions of cloud-top evolution during plume formation by Fujita (1982), where it was given the name "jumping cirrus." In addition to wave breaking, some studies suggest that the stability of the lower stratosphere may influence above-anvil cirrus plume formation. In particular, simulations of tropopause-penetrating convection within relatively low (near tropospheric)-stratospheric stability environments have been shown to produce plumes (e.g., Homeyer et al. 2014a). Homeyer et al. (2014a) suggest that reduced lower-stratospheric stability enables an ascending convective parcel to become neutrally buoyant at stratospheric altitudes, detrain laterally in the direction of the prevailing wind, and remain above the broader anvil cloud (i.e., form a plume).

If above-anvil cirrus plumes do represent stratospheric injection of clouds and, upon their sublimation, water vapor, they may have significant impacts on the composition of the upper troposphere and lower stratosphere (UTLS) and climate. Namely, water vapor is a powerful greenhouse gas, with increases in stratospheric water vapor leading to a cooling of the stratosphere and a warming of Earth's surface (e.g., Forster and Shine 1999; Solomon et al. 2010). Anderson et al. (2012) argue that increases in stratospheric water vapor from convection can lead to the activation of organic chlorine to free radical form and subsequent destruction of stratospheric ozone, which is also a greenhouse gas whose radiative impact is most sensitive to changes in UTLS composition (e.g., Lacis et al. 1990). Furthermore, stratospheric ozone helps to block harmful UV radiation from reaching Earth's surface. Thus, decreases in its concentration from water vapor injection will lead to negative impacts on human health and a reduction in the rate of warming at Earth's surface. Model projections of the future do suggest that convective available potential energy (CAPE, a measure of instability) and convective updraft speeds will increase in a warming climate, such that tropopause-penetrating convection and stratospheric injection may be more likely if changes in the altitude of the tropopause are relatively small (e.g., Del Genio et al. 2007; Trapp et al. 2007; Romps et al. 2014; Trapp and Hoogewind 2016).

The association of above-anvil cirrus with the enhanced-V satellite signature is not the only established linkage with severe weather. In the study by Bedka et al. (2015), satellite observations of above-anvil cirrus plumes predicted severe weather with an average lead time of 18 min. However, despite this association, it is not known how often convection produces both visible above-anvil cirrus plumes and enhanced-V signatures or how often they occur separately.

The association of above-anvil cirrus plumes with stratospheric injection of clouds and with occurrences of severe weather provides motivation for a deeper understanding of their formation, maintenance, and additional characteristics. This study focuses on establishing such an understanding by analyzing a unique set of observations and model output, including high-resolution satellite imagery, four-dimensional ground-based radar observations, assimilations of the atmospheric state from a state-of-the-art reanalysis model, and idealized simulations for cases of deep convection with and without above-anvil cirrus plumes. We seek to answer several questions, including: 1) do above-anvil cirrus plumes *always* represent the injection of cloud particles into the lower stratosphere (i.e., rather than vertically displaced cloud layers within the troposphere or in situ formation of cirrus in the stratosphere due to cooling from the overshooting convective top)?, 2) what convective and/or environmental characteristics are conducive to above-anvil cirrus plumes?, and 3) can observed relationships between above-anvil cirrus plumes and convective/environmental characteristics be reproduced in a numerical model?

2. Data

a. Satellite imagery

To enable the detection of above-anvil cirrus, we use satellite imagery from the National Oceanic and Atmospheric Administration (NOAA) Geostationary Operational Environmental Satellite (GOES) constellation

(Menzel and Purdom 1994). GOES is primarily a system of two operational satellites that continuously monitor the weather over the United States: GOES-West stationed at 135°W longitude and GOES-East at 75°W longitude. Data for each storm were obtained from NOAA through the Comprehensive Large Array-Data Stewardship System (CLASS; NOAA 1994). For the cases analyzed in this study, imagery is routinely available at 5–30-min intervals when using observations from both GOES-West and GOES-East. We employ both visible and infrared (IR) imagery in this study. The visible imager aboard the current generation of GOES satellites has a horizontal resolution of 1 km at nadir, while the IR imager has a horizontal resolution of 4 km at nadir and an absolute accuracy of ≤1 K. We compute brightness (cloud top) temperatures using the IR channel 4 wavelength band (10.2–11.2 μm).

b. Radar observations

Radar observations from the Next Generation Weather Radar (NEXRAD) program Weather Surveillance Radar-1988 Doppler (WSR-88D) network are used to evaluate the physical and dynamical characteristics of each storm, including their height, intensity, and motion (Crum and Alberty 1993). Volumes from individual radars were obtained from the National Centers for Environmental Information (NCEI, formerly the National Climatic Data Center) and typically available at 4–10-min increments (NOAA/NWS/ROC 1991). For analysis, we bin the radar observations in space and time on a large-area grid using methods similar to that outlined in Homeyer (2014) and Homeyer and Kumjian (2015), which provides four-dimensional radar composites at a longitude–latitude resolution of 0.02° (~2 km), a vertical resolution of 1 km, and a temporal resolution of 5 min. Although the radar data provide several microphysical and dynamical variables for analysis, we use a single radar variable in this study: the radar reflectivity at horizontal polarization Z_H (dBZ), which provides information on the size and/or concentration of precipitable hydrometeors within a storm. In particular, many of our analyses rely on composite Z_H echo-top altitudes, which have an uncertainty of 500–1000 m based on comparisons with higher-resolution vertically pointing radar systems [e.g., see Fig. 6 of Homeyer (2014)].

c. Model analyses

Assimilated atmospheric states from the European Centre for Medium-Range Weather Forecasts (ECMWF) interim reanalysis (ERA-Interim) are used to examine the characteristics of the atmospheric environment in the vicinity of each storm (Dee et al. 2011). ERA-Interim output was obtained at 6-h intervals on a horizontal Gaussian grid with a longitude–latitude resolution of 0.75° × ~0.75° (~80 km) and at 60 native model levels in the vertical on a hybrid sigma–pressure grid from the National Center for Atmospheric Research (NCAR) Research Data Archive (RDA; ECMWF 2009). Linear horizontal and temporal interpolation and cubic-spline interpolation in the vertical is used in this study to project temperature and winds from ERA-Interim onto the path of each storm.

3. Methods

a. Case selection

Based on the known association between severe weather and above-anvil cirrus plume occurrence (e.g., Bedka et al. 2015), cases used in this study were selected following a three-step process. First, random days with a large number of severe weather reports (greater than 75) were identified using the NOAA Storm Prediction Center (SPC) severe weather report archive (http://www.spc.noaa.gov/climo/online/). Second, visible imagery from NCAR's Mesoscale and Microscale Meteorology (MMM) laboratory online archive (http://www2.mmm.ucar.edu/imagearchive/) was analyzed to identify possible above-anvil cirrus plume occurrences. Third, GOES imagery at full resolution was obtained and analyzed to confirm or deny the presence of above-anvil cirrus plumes. Once confirmed, WSR-88D observations and ERA-Interim were obtained for complete analysis of each event. Identification of tropopause-penetrating convection without above-anvil cirrus plumes was similar. Table 1 lists all 20 daily events and the number of storms from each case with and without above-anvil cirrus plumes analyzed in this study.

b. Above-anvil cirrus plume detection

To identify cirrus clouds lying above the anvils of convection, we use a combination of objective and subjective techniques with GOES imagery. In particular, the primary method of identification is based on varying the black–white contrast of each visible image to adjust for solar illumination of the cloud top and reveal shadows cast by the cirrus clouds on the anvil below. This method enabled plume identification in almost all cases used in this study. In the absence of shadowing or based on a need for confirmation of questionable features, above-anvil cirrus were further identified as distinct variations in visible texture or IR temperature of the cloud top, where the above-anvil cirrus tend to be less textured (smoother) and warmer than the broader anvil cloud (e.g., Setvák and Doswell 1991; Levizzani and Setvák 1996; Bedka et al. 2015). A limited number of storms used in this study required this second step, and all storms passed at least two

TABLE 1. Case dates, states included (domain), and the number of storms used for analysis of convection with and without above-anvil cirrus plumes.

Date	States included	No. storms with plumes	No. storms without plumes
8 May 2013	KS, OK	4	3
17 May 2013	TX	2	0
18 May 2013	KS, NE, OK, TX	2	4
27 May 2013	KS, NE	2	0
28 May 2013	KS, OK	2	1
29 May 2013	OK, TX	0	5
31 May 2013	IL, KS, MO	0	6
27 Jun 2013	KS, OK, TX	0	6
21 Aug 2013	WI	1	0
3 Apr 2014	OK, TX	3	0
12 Apr 2014	IA, KS, NE	3	0
28 Apr 2014	AL, LA, MS	0	7
7 May 2014	OK, TX	3	0
20 May 2014	CO, KS, NE	1	0
3 Jun 2014	IA, KS, MO, NE	2	0
5 Jun 2014	CO, KS	1	0
14 Jun 2014	KS, NE	3	2
8 Apr 2015	KS, OK, TX	2	4
6 May 2015	KS, OK, TX	3	0
7 May 2015	OK, TX	0	3
Total storms		34	41

of these three criteria. Figure 1 shows examples of visible imagery for two cases used in this study: Fig. 1a, representing an above-anvil cirrus plume case, and Fig. 1b, representing a case with no above-anvil cirrus plumes.

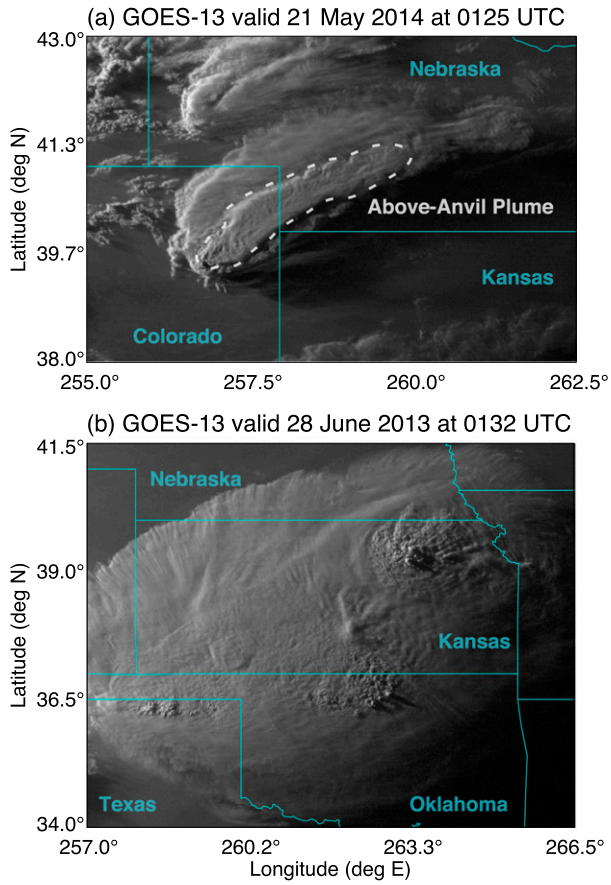

FIG. 1. Maps of GOES 1-km visible imagery for (a) an above-anvil cirrus plume case valid at 0115 UTC 21 May 2014 and (b) an overshooting (tropopause penetrating) convection case without above-anvil cirrus plumes valid at 0132 UTC 28 Jun 2013. State boundaries are shown by the cyan lines, and the thick dashed white line in (a) illustrates the extent of the observed above-anvil cirrus plume.

c. *Storm tracking*

To track individual storms to determine their motion and additional physical characteristics, we developed a novel algorithm that leverages the volumetric information available in the WSR-88D composites. Prior studies have employed techniques that track low-level radar reflectivity maxima using only plan-view observations or storm volume estimates from a single radar [so-called centroid or object-based methods (e.g., Rosenfeld 1987; Dixon and Wiener 1993; Johnson et al. 1998; Handwerker 2002; Han et al. 2009)]. These object-based methods typically follow a four-step procedure: 1) identify local maxima in reflectivity at each elevation of a radar volume, 2) define centroids (closed contours) that best represent and/or isolate individual storms, 3) link centroids in consecutive radar scans by closeness (time increment is typically required to be less than 20 min between scans), and 4) retain storm identifications that have vertical continuity (i.e., can be identified at more than one radar elevation). These algorithms, while often successful, have been shown to identify too few or too many storms, suffer when applied to merging or splitting storms, and provide conflicting estimates of storm motion. Most of these difficulties can be argued to be a result of the scanning limitations of a single radar (both resolution and geometry).

Our approach is to provide a simpler and reliable alternative to object-based storm tracking that can be applied to volumetric, large-area datasets such as the radar composites used in this study. In particular, we track storms by identifying local maxima in radar echo-top altitudes, which are taken to be a proxy (or estimate) of updraft locations within deep convection. This algorithm provides continuous storm tracks using a three-step procedure: 1) identify local maxima of the Z_H = 30-dBZ echo top that exceed the altitude of the environmental melting (or freezing) level, 2) link maxima in consecutive radar volumes if within 15 km of each other at a time increment ≤5 min (based on iterative threshold evaluations in a wide variety of cases), and 3) retain tracks that are at least 15 min in duration for

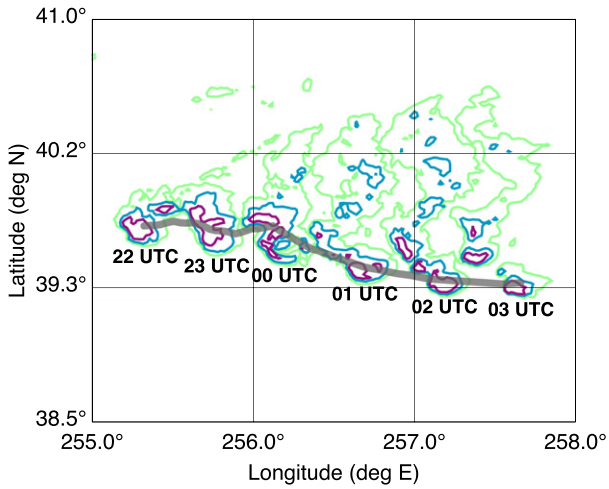

FIG. 2. Map of WSR-88D column-maximum (composite) radar reflectivity at 1-h increments beginning at 2200 UTC 20 May 2014 and the echo-top-based storm track (thick gray line) for the above-anvil cirrus plume–producing storm in northeastern Colorado shown in Fig. 1a. Radar reflectivity contours are 30 (green), 40 (blue), and 50 (purple) dB*Z*.

analysis. Analyses of individual storm characteristics in this study include radar observations within 15 km of the echo-top-based storm tracks. Figure 2 shows an example storm track generated using the echo-top algorithm for the above-anvil cirrus plume case in Fig. 1a. Radar reflectivity maxima at hourly increments in Fig. 2 coincide well with the storm track from the echo-top algorithm and establish confidence in its performance.

To further demonstrate the performance of the echo-top storm tracking algorithm, we present a comparison of storm motion computed using the echo-top method and that from the operational object-based storm tracking method applied to individual WSR-88D observations in Fig. 3. The operational storm tracks were produced using storm cell identifications obtained from NOAA's Severe Weather Data Inventory (SWDI; http://www.ncdc.noaa.gov/swdi/). Fig. 3a shows frequency distributions of the mean storm motion along individual storm tracks from each method. These frequency distributions correspond to observations for the 5–6 June 2014 case in the vicinity of the Pueblo, Colorado, WSR-88D [International Civil Aviation Organization (ICAO) station KPUX] and include 27 storm tracks from the echo-top algorithm and 75 storm tracks from the SWDI archive. Both sets of storm tracks contain only those that have lengths ≥15 min, with the difference in the number of storms and their track lengths (see Fig. 3b) largely related to the restriction of echo-top tracking to storms exceeding the melting-level altitude. These distributions show that the storm motions calculated from the two tracking methods are similar, with a mode that is slightly faster in the echo-top-based tracks, possibly because of the exclusion of weaker storms. The map of the two storm-track populations (Fig. 3b) also demonstrates similar performance of the two methods, with long-duration storm-track coordinates being nearly coincident. Comparisons of the two tracking methods at additional radar locations and for alternative cases examined in this study are consistent with this example.

d. Idealized simulations

To test results from the analysis of multiple observational datasets in this study, we conducted two idealized simulations of explicitly resolved tropopause-penetrating convection with version 3.7.1 of the Advanced Research version of the Weather Research and Forecasting (WRF-ARW) Model (Skamarock et al. 2008). The idealized simulations consisted of modifications to the quarter-circle-shear supercell configuration provided in the public WRF distribution. Additional details on the nature of the modification in each simulation are provided in section 4b. For each simulation, the horizontal resolution was 1 km, and the grid size was 600 km × 600 km. The model top was set at 25 km, and the vertical resolution was 150–250 m (141 vertical levels), with a damping layer employed within 5 km of the model top to prevent reflection of spurious waves. Model simulations were output at 15-min intervals for analysis. There are many choices for parameterization of physical processes in WRF. The simulations in this study employed the NSSL two-moment four-ice microphysics parameterization with predicted cloud condensation nuclei (Mansell et al. 2010) and the RRTM for GCM applications (RRTMG) parameterization for shortwave and longwave radiation (Iacono et al. 2008). No planetary boundary layer or cumulus parameterizations were used.

e. Tropopause identification

For determining the altitude of the tropopause in the ERA-Interim output and WRF simulations, we employ the World Meteorological Organization (WMO) lapse-rate definition (WMO 1957). Specifically, the altitude of the tropopause is defined as "the lowest altitude at which the temperature lapse rate decreases to 2 K km^{-1}, provided that the average lapse rate from this level to any point within the next higher 2 km does not exceed 2 K km^{-1}." The WMO definition is preferred in this study because of its superiority over alternative methods, such as potential vorticity (PV) isosurfaces, in the vicinity of convection (where alternatives are ill defined) and its common coincidence with the chemical transition from troposphere to stratosphere (e.g., Gettelman et al. 2011; Homeyer et al. 2014a). While the vertical resolution of ERA-Interim is low compared to balloon observations

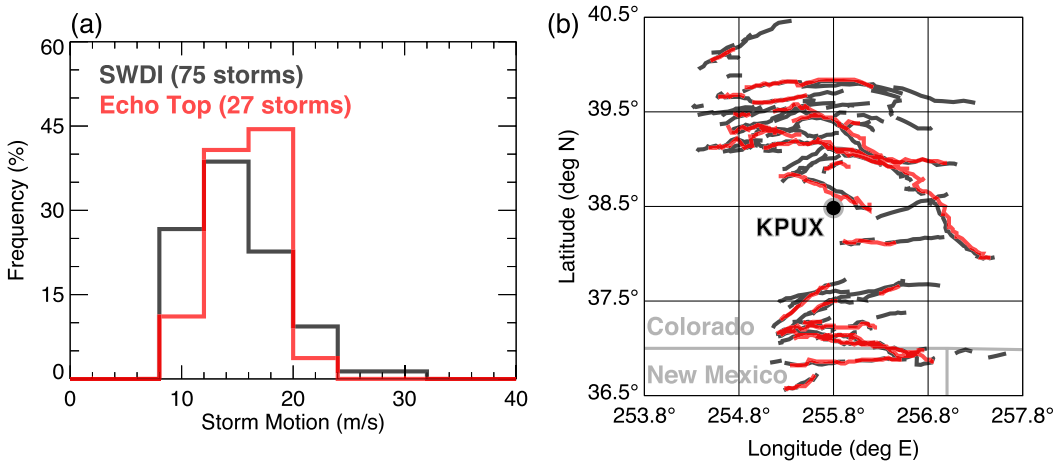

FIG. 3. Comparison of radar-based storm tracking methods applied to the 5 Jun 2014 case showing (a) a frequency distribution of the mean storm motion along individual tracks and (b) a map of the individual tracks. Black lines correspond to storm tracks from the SWDI archive, and red lines correspond to those from the echo-top algorithm used in this study. In (b), state boundaries are shown by the thick gray lines and the Pueblo, Colorado, WSR-88D radar location (KPUX) is shown by the gray and black labeled circle.

and the WRF simulations employed in this study, it has been shown to represent the altitude of the WMO tropopause well when compared to that from high-resolution radiosondes, with a typical uncertainty of ~500 m (e.g., Homeyer 2014; Solomon et al. 2016).

4. Results

a. Observations

To first examine the argument that above-anvil cirrus plumes represent the injection of cloud particles into the stratosphere, we compare the $Z_H = 10$-dBZ radar echo-top altitude to the altitude of the ERA-Interim tropopause along the path of each observed storm. Frequency distributions of the resulting maxima in tropopause-relative altitude are given in Fig. 4. This analysis demonstrates that all storms with above-anvil cirrus plumes penetrate the tropopause and supports the assertion that plumes represent stratospheric injection. Thus, in order to facilitate further analysis of these storms and identification of unique characteristics associated with storms that produce above-anvil cirrus plumes, we include equivalent analyses of a similar population of tropopause-penetrating convection without above-anvil cirrus plumes in the remainder of this section. The tropopause-relative altitude distribution of that population is also given in Fig. 4.

Examining the formation of above-anvil cirrus clouds is a potentially complex problem. Based on previous studies and the initial finding of this study that all plume cases likely represent stratospheric injection, several hypotheses can be developed to explain their formation. These include: 1) the stability of the stratosphere must be low (i.e., near tropospheric), 2) the storm-relative horizontal wind in the UTLS must be large such that frequent gravity wave breaking and/or rapid deformation (i.e., stretching) of the overshooting top occurs, 3) the storm must frequently penetrate or remain above the tropopause for a long period of time to provide a near-continuous source of cloud particles so that a plume can be maintained, and 4) the stratosphere prior to convective penetration is near saturation such that cooling induced by the overshooting top leads to in situ formation of cirrus rather than convective injection. To evaluate the role of these mechanisms, we first compare the suite of observations or observation-based datasets employed in this study for storms with and without above-anvil cirrus plumes.

Figure 5 shows mean tropopause-relative profiles of ERA-Interim temperature and the magnitude of vector differences between ERA-Interim horizontal wind $\hat{U}_H$ and the storm motion $\hat{U}_S$ from our echo-top storm tracking algorithm along the path of each storm (where each profile is colored by the corresponding storm's maximum tropopause-relative echo-top altitude). Both populations of storms occur within a similar envelope of stratospheric stability environments (Figs. 5a,c), with the largest decreases in temperature above the tropopause (and consequently lowest stratospheric stability) found in the environments of storms without above-anvil cirrus plumes. Despite similarity in the stratospheric stability envelope, the tropopause inversion layer is slightly stronger overall (i.e., more stable) in the population of storms without above-anvil cirrus plumes (but not statistically significant). This suggests that the

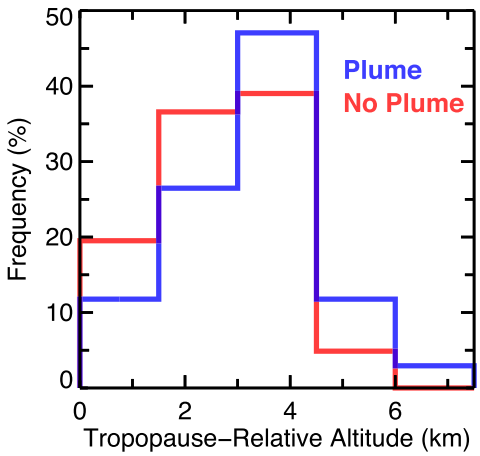

FIG. 4. Frequency distributions of the maximum tropopause-relative altitude (or overshooting depth) of observed storms. Cases with above-anvil cirrus plumes are given by the blue line and cases without by the red line.

stability of the stratosphere is not necessarily important to the formation of above-anvil cirrus, despite its known influence of increasing the depth of tropopause penetration (e.g., Homeyer et al. 2014b; Solomon et al. 2016). Differences in the overshooting depth are apparent in the two populations, with overshoots commonly higher in storms with above-anvil cirrus plumes (similar differences are seen in the frequency distributions of Fig. 4). In contrast to stratospheric temperature, profiles of storm-relative horizontal wind (Figs. 5b,d) show clear and consistent differences between the populations of tropopause-penetrating storms with and without above-anvil cirrus plumes. Specifically, storm-relative wind speeds range mostly from 5 to 25 m s^{-1} in the first 2–3 km above the tropopause for cases without above-anvil cirrus plumes, while they range mostly from 15 to 35 m s^{-1} in cases with plumes. Using a Student's t test, we find that the two populations of storm-relative wind profiles are significantly different at the 99% level from tropopause-relative altitudes of −2 to 4 km (not shown).

While differences in storm-relative wind are readily apparent in the two populations of tropopause-penetrating storms, there is considerable overlap such that no single value separates them. It is possible that this overlap is an artifact of the combined uncertainty in storm motion and ERA-Interim winds, but it is equally possible that this could be a real characteristic. To examine these differences in greater detail, we present component analysis of the winds in Fig. 6 and an alternative approach to the stability–storm-relative wind analysis in Fig. 7. In particular, Fig. 6 shows wind vector scatterplots (speed and direction) for the radar-derived storm motion and lower-stratosphere wind from ERA-Interim (that at 1 km above the tropopause). These plots demonstrate that both slower storm motion and faster lower-stratosphere wind contribute to the larger storm-relative wind speeds observed in above-anvil cirrus plume cases. Figure 7 shows scatterplots of each storm population as a function of both stratospheric stability (given as the mean vertical temperature gradient in the first 4 km above the tropopause) and storm-relative lower-stratosphere wind (at 1 km above the tropopause, as in Fig. 6). These scatterplots reveal the codependency of the observed storms on stratospheric stability and storm-relative wind. The relationship between stronger storm-relative wind and above-anvil cirrus plume occurrence identified in Fig. 5 is evident in Fig. 7 by the areas where the two storm populations do not overlap. The tendency of storms with plumes to occur in environments with lower stratospheric stability is also evident. These distributions further demonstrate that tropopause-penetrating convection with above-anvil cirrus plumes tends to be about 2 km deeper than that without plumes (in a tropopause-relative sense) in areas where the two distributions do overlap. Thus, while strong storm-relative wind in the lower stratosphere (>25 m s^{-1}) appears to be indicative of above-anvil cirrus plume occurrence, the depth of stratospheric penetration and/or stratospheric stability may also play an important role, especially when the storm-relative wind is of moderate strength (15–25 m s^{-1}).

The differences in storm-relative wind found between the two populations suggest that stretching of the overshooting top or the frequency of gravity wave breaking is larger in storms with above-anvil cirrus plumes. As outlined in previous studies, gravity waves generated in convection are expected to break (and lead to mixing and/or lofting of cloud particles into the lower stratosphere) where the storm-relative horizontal wind speed is greater than or equal to the phase speed of the wave (e.g., Lane et al. 2003; Lane and Knievel 2005). These studies also show that numerical simulations of tropopause-penetrating convection generate gravity wave spectra that scale with the horizontal grid resolution of the model, such that it is not known what resolution is appropriate for generating spectra representative of real (i.e., observed) convection (see also Lane and Moncrieff 2008). Coarser grid resolutions (on the order of 1 km) are found to result in convectively generated gravity waves with longer wavelengths and faster phase speeds, while finer grid resolutions are found to result in convectively generated gravity waves with shorter wavelengths and slower phase speeds and, thus, more frequent wave breaking. Therefore, based on the differences in storm-relative UTLS wind found for the observed storms analyzed here, it is expected that gravity wave breaking will be more frequent in storms with above-anvil cirrus

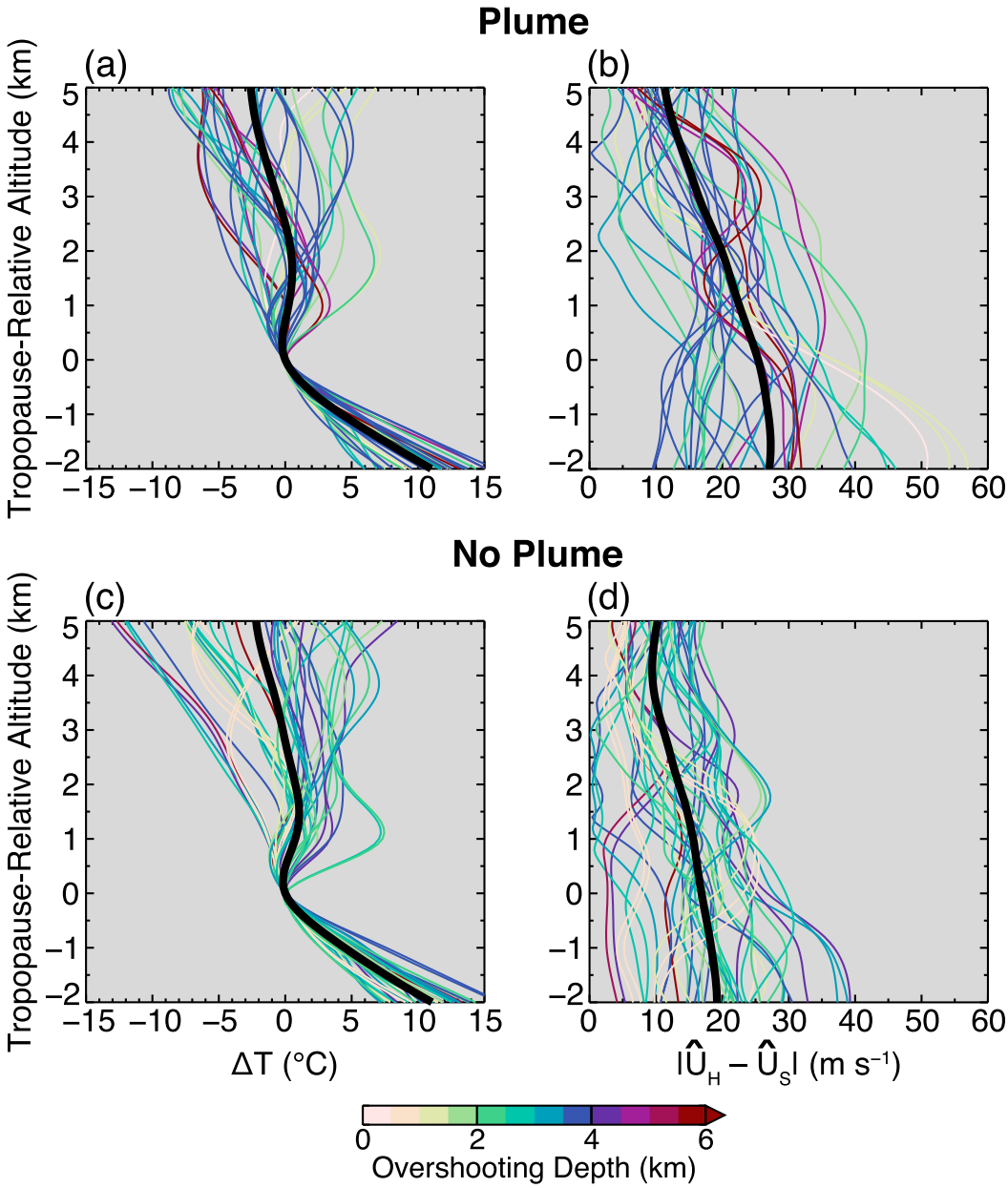

FIG. 5. From ERA-Interim, environmental profiles at relative altitudes to the tropopause of (a),(c) tropopause-relative temperature ΔT (°C) and (b),(d) storm-relative horizontal wind speed $|\hat{U}_H - \hat{U}_S|$ (m s^{-1}) for observed storms (a),(b) with and (c),(d) without above-anvil cirrus plumes. Profiles for each storm are colored by its maximum tropopause-relative altitude (overshooting depth). Mean profiles are given as thick black lines in each panel.

plumes. It may also be the case that stretching of the overshooting top is more rapid and an important contributor to the formation and maintenance of above-anvil cirrus. However, the significance of these mechanisms for above-anvil cirrus plume formation cannot be adequately addressed using the observational datasets available to this study. To better evaluate these processes, we revisit this topic in the analysis of the idealized model simulations in section 4b.

Based on the typical scale and continuity of above-anvil cirrus plumes observed in satellite imagery, an association of their occurrence with a storm's duration of tropopause penetration is a strong hypothesis. Thus, we employ the output from the radar echo-top storm tracking algorithm here to examine this potential relationship. Figures 8a and 8b show frequency distributions (for both storm populations) of the trackable lifetime of storms and the percentage of that lifetime a

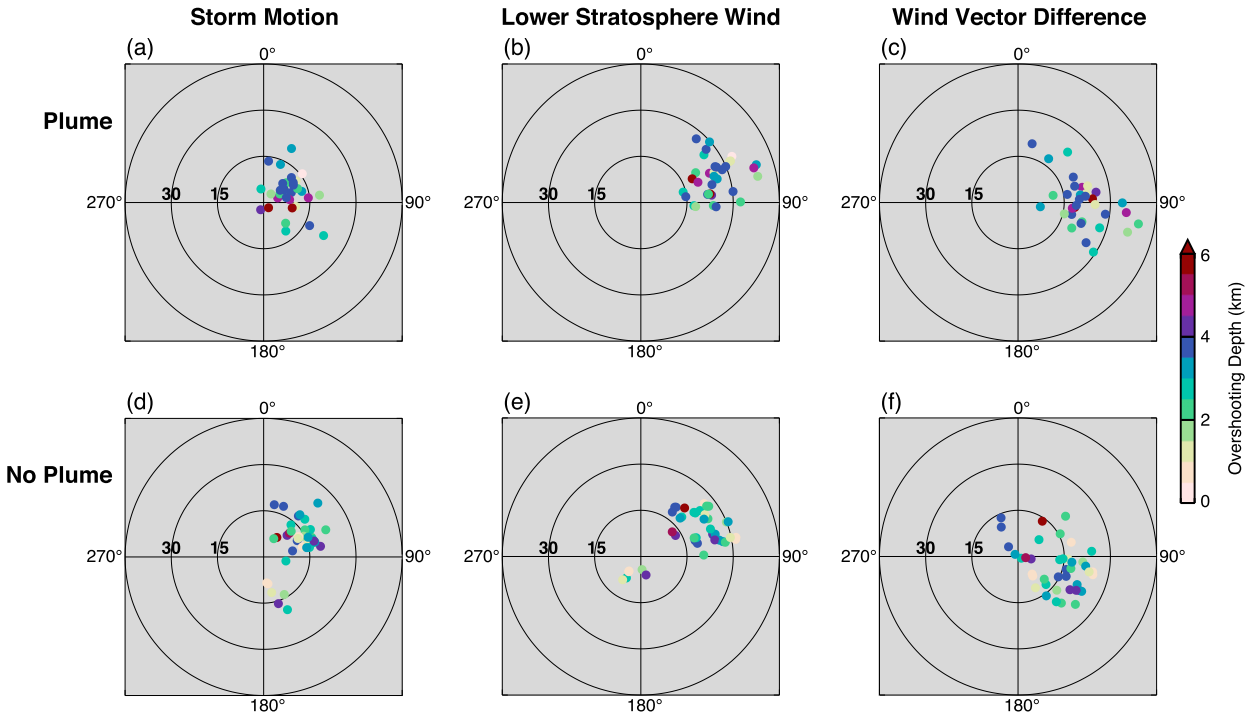

FIG. 6. Wind vector scatterplots showing (a),(d) storm motion, (b),(e) lower-stratosphere environmental wind (at 1 km above the tropopause from ERA-Interim), and (c),(f) the environmental wind minus storm motion vector difference for observed storms (a)–(c) with and (d)–(f) without above-anvil cirrus plumes. Wind speed (radii) is in meters per second and direction in degrees (azimuth), where the convention of 0° being toward the north is used. Each storm is given as a circle colored by its maximum tropopause-relative altitude (overshooting depth).

storm's echo top exceeds the altitude of the tropopause, respectively. These distributions show that most storms analyzed here have a trackable lifetime of 1–4 h, with the lifetime of plume-producing storms being slightly longer. Despite the slight offsets in lifetime between the two populations, both show similar durations of tropopause penetration during their lifetime, with typical values in excess of 60%. Thus, the formation of an above-anvil cirrus plume does not simply require that a storm spends most of its lifetime reaching into the stratosphere. Similar comparisons are found when looking at lengths of continuous tropopause penetration for each storm, which range from 5 to 20 min (not shown).

Finally, it is possible that the humidity of the lower stratosphere would impact the formation of above-anvil cirrus plumes. In particular, if the stratosphere is near saturation prior to convective penetration, cooling induced by the convective overshoot could lead to the generation of excess vapor and nucleation of ice particles and therefore in situ formation of cirrus rather than injection of cloud material from the convective overshoot. While there is little valuable information on stratospheric humidity from ERA-Interim and other model analyses [e.g., see Jiang et al. (2015), and references therein], temperature can be used as a reasonable proxy in its place. In particular, since we know that the extratropical lower-stratosphere water vapor concentration is commonly within a tight range of 5–10 ppmv and significant perturbations above this range are almost always due to convection, we can compare the temperature of the environment to a given frost-point temperature to determine the likely stratospheric humidity. If we assume the upper bound of the common range of extratropical lower stratosphere water vapor (i.e., 10 ppmv), the frost-point temperature from the Clausius–Clapeyron equation would be about −80°C at extratropical stratospheric altitudes. Thus, in order for the stratosphere to be near saturation and in situ cirrus formation to be possible, the temperature must be within a few degrees of this value. For the observed tropopause-penetrating convection analyzed in this study, ~90% of the tropopause temperatures from ERA-Interim are −60° ± 5°C and no tropopause temperature falls below −70°C. This characteristic, taken together with the temperature profiles of Fig. 5, demonstrates that none of our analyzed storms occur within stratospheric environments near saturation. Therefore, we find in situ formation of above-anvil cirrus plumes to be unlikely in extratropical storms.

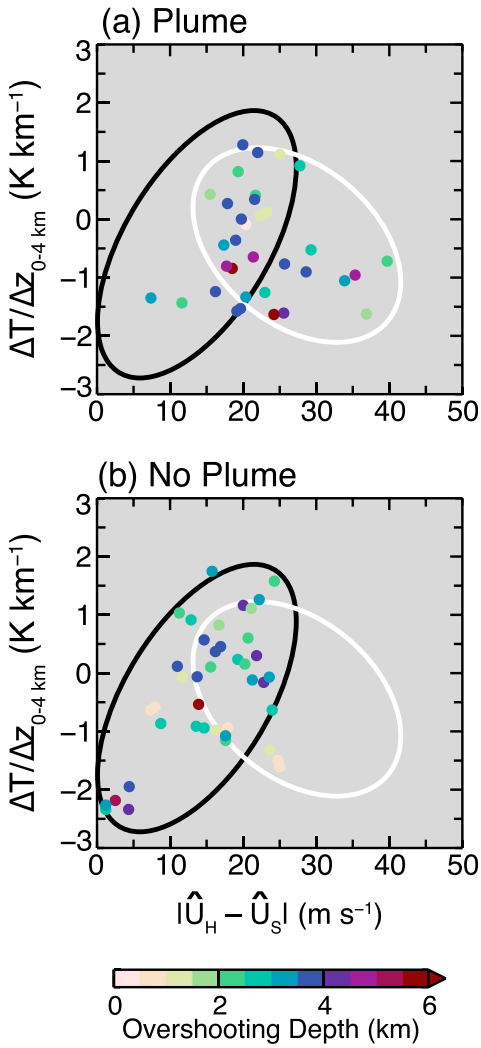

FIG. 7. Scatterplots of storms (a) with and (b) without above-anvil cirrus plumes, as a function of storm-relative wind at 1 km above the tropopause (abscissa) and the mean vertical temperature gradient in the 4 km above the tropopause (ordinate), which is a measure of stratospheric stability. The black ellipses in each panel encompass the main population of storms without above-anvil cirrus plumes, and the white ellipses encompass the main population of storms with above-anvil cirrus plumes. Each storm is given as a circle colored by its maximum tropopause-relative altitude (overshooting depth).

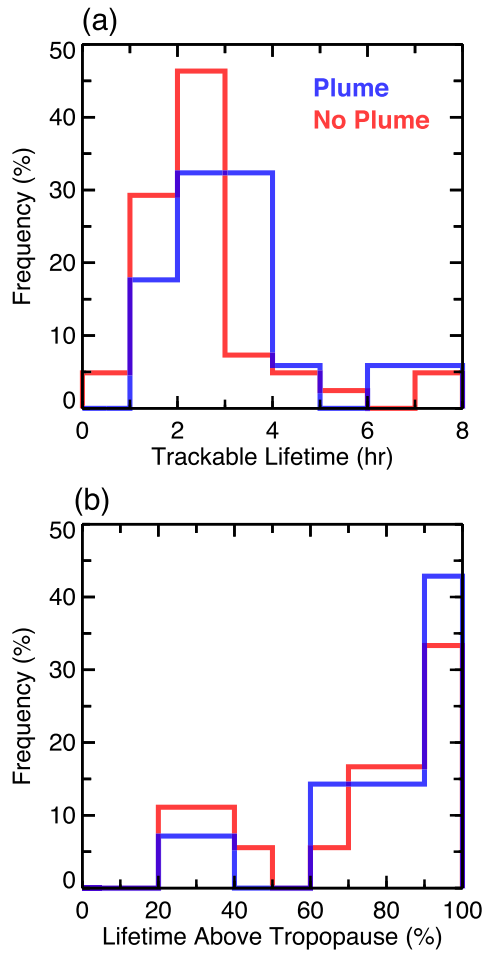

FIG. 8. As in Fig. 4, but for (a) the trackable lifetime of the storm and (b) the fraction of tracked lifetime where the storm top exceeded the altitude of the tropopause.

b. Simulations

As demonstrated in the observational analysis given in section 4a, above-anvil cirrus plumes are most clearly associated with relatively large storm-relative winds in the UTLS. In this section, we examine the ability of a numerical model to reproduce this relationship and the mechanisms by which it is established. We present the results of two individual idealized WRF simulations here, which are initialized with equivalent thermodynamic environments (instability, moisture, and tropopause altitude) and differing UTLS wind profiles. The simulations are based on the quarter-circle-shear supercell configuration provided in the public WRF distribution, which uses an idealized meteorological profile based on that in Weisman and Klemp (1982). The tropopause altitude of the idealized profile is 12 km.

There are two important differences between our idealized profiles and that provided in the WRF distribution. First, the water vapor mixing ratio in both idealized profiles was modified to be physically representative of the stratosphere (i.e., consistent with observations). In particular, we let the water vapor mixing ratio decrease to 5 ppmv in the first 2 km of the lower stratosphere and remain constant at 5 ppmv above, while the original idealized profile holds relative humidity fixed at altitudes above the tropopause, leading to artificial hydration of the stratosphere and water vapor mixing ratios in excess of 35 ppmv at altitudes

above 14 km and 100 ppmv at altitudes above 19.5 km. Second, we modify the wind profile in each simulation to produce characteristically different storm-relative wind profiles in the UTLS. Namely, we first increase the magnitude of the original winds in the idealized profile by 50% to produce a single right-moving supercell. This approach also aims to achieve large storm-relative winds and thus a storm with an above-anvil cirrus plume. For the second simulation, we reduce the wind speeds by approximately 50% in the profile at altitudes from 1 km below the tropopause (i.e., 11 km) to the model top. In addition to reducing the wind speed, the wind direction is veered to align with the storm motion realized in the first simulation, aiming to thus achieve small storm-relative winds and no above-anvil cirrus plume. Both of these profiles and the precise model configuration settings are provided as supplemental material to this manuscript.

The two idealized simulations were successful in simulating convection of similar intensity (as expected based on equivalent thermodynamic environments) and evolution, reaching altitudes up to 3 km above the convectively elevated tropopause in the convective core (up to an altitude of ~16 km). The goal of achieving storm-relative winds characteristic of the two observed populations of tropopause-penetrating convection was also met. Storm-relative winds in the simulation intended to be representative of the above-anvil cirrus plume cases are $\geq 30\,\mathrm{m\,s^{-1}}$, and those in the simulation intended to be representative of the cases without plumes are $\leq 15\,\mathrm{m\,s^{-1}}$. In addition, the observed relationship between the development of above-anvil cirrus plumes and relatively large storm-relative UTLS winds was reproduced. Figure 9 demonstrates these findings via maps of simulated radar reflectivity at an altitude of 85 m above the surface and cloud-top altitudes relative to the tropopause of the two idealized WRF simulations at 45-min intervals. One important aspect to note here is that, while the cloud-top altitudes are similar within the convective cores in each simulation, the cloud-top altitudes of the simulated above-anvil cirrus plume are considerably higher (up to ~5 km above the tropopause).

Based on the success of the model simulations in reproducing the observed relationship between above-anvil cirrus plume formation and relatively large storm-relative wind speeds, we can further examine the simulations to identify the mechanisms responsible for this relationship. In particular, we seek to examine the role of gravity wave generation and breaking in plume formation and maintenance versus rapid deformation (or stretching) of the overshooting convective top. Figure 10 shows vertical cross sections through the supercells in the simulations with and without an above-anvil cirrus plume. In each cross section, contours of potential temperature (isentropes) at 5-K intervals are shown in order to facilitate identification of gravity waves and wave breaking. Gravity waves can be identified as coherent mesoscale vertical undulations in the altitudes of isentropes and wave breaking as vertical overturning of isentropes. The cross sections show that vertically propagating gravity waves are generated in both simulations, with clear undulations of isentropes above the simulated storms. The undulations are largest in the simulation with an above-anvil cirrus plume. However, only the simulation with an above-anvil cirrus plume shows evidence of gravity wave breaking and lofting of the cloud top to an altitude of ~17 km at this time. In fact, such gravity wave breaking is present in the near vicinity of the convective core at every model analysis time following the first instance of tropopause penetration. Figure 11 summarizes this wave breaking activity through cumulative counts of unstable layers within cloud during each simulation (i.e., negative vertical potential temperature gradients in 15-min model output volumes) as a function of relative altitude to the tropopause. These profiles demonstrate that gravity wave breaking is observed in both simulations but only occurs commonly within the overshooting top in the simulation with an above-anvil cirrus plume. Although stretching of the overshooting top may also contribute to above-anvil cirrus plume formation, these results suggest that irreversible mixing due to frequent gravity wave breaking is the primary mechanism responsible.

The vertical cross sections (Fig. 10) also demonstrate that irreversible injection of water vapor to stratospheric potential temperature levels (predominantly from ice sublimation) is observed in both simulations, with deeper injection in the storm with an above-anvil cirrus plume. Figure 12 provides a more quantitative measure of irreversible injection of water into the lower stratosphere. In particular, mean profiles of water vapor as a function of potential temperature are given based on output from the final simulation time and correspond to a 300 km × 300 km box centered on the supercell storm in each simulation. The initial water vapor profile is also given for comparison. These water vapor profiles reveal a stark contrast of the impact of each simulated storm on the humidity of the lower stratosphere, with minor, nearly indistinguishable enhancements in stratospheric water up to ~405 K in the simulation without an above-anvil cirrus plume and large enhancements (up to a doubling of the initial water vapor concentration) in stratospheric water up to ~440 K in the simulation with an above-anvil cirrus plume. Thus, although extratropical tropopause-penetrating convection may always lead to an increase in stratospheric water vapor, gravity wave

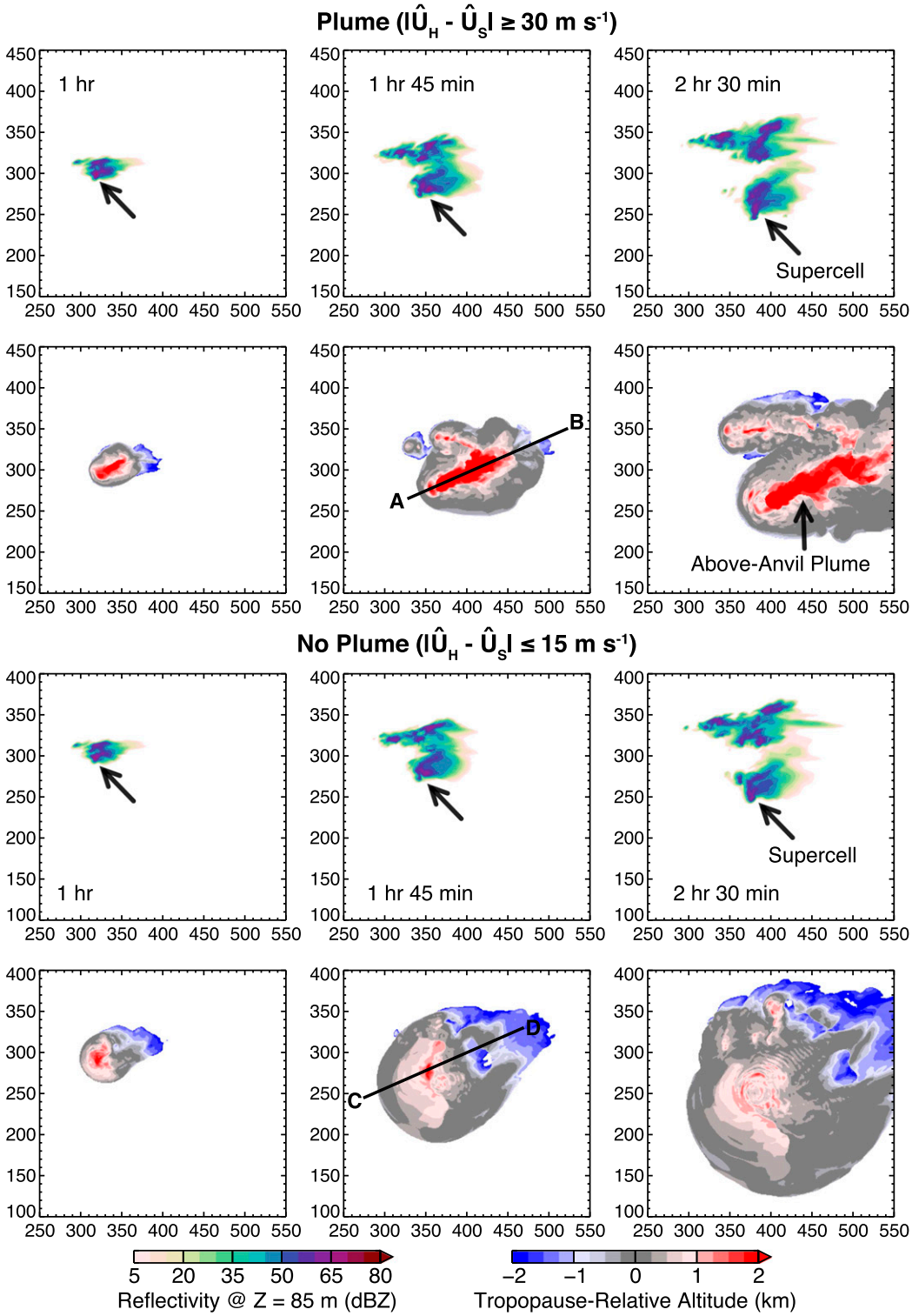

FIG. 9. From idealized WRF simulations, simulated radar reflectivity at an altitude of 85 m AGL and tropopause-relative cloud-top altitudes (cloud particle mixing ratio $\geq 0.01\ \mathrm{g\,kg^{-1}}$) at 45-min increments for simulations with stratospheric storm-relative wind speeds (top) ≥ 30 and (bottom) $\leq 15\ \mathrm{m\,s^{-1}}$. Grid axes are in kilometers. The thick black lines labeled "A–B" and "C–D" show the locations of the vertical cross-sections given in Fig. 10.

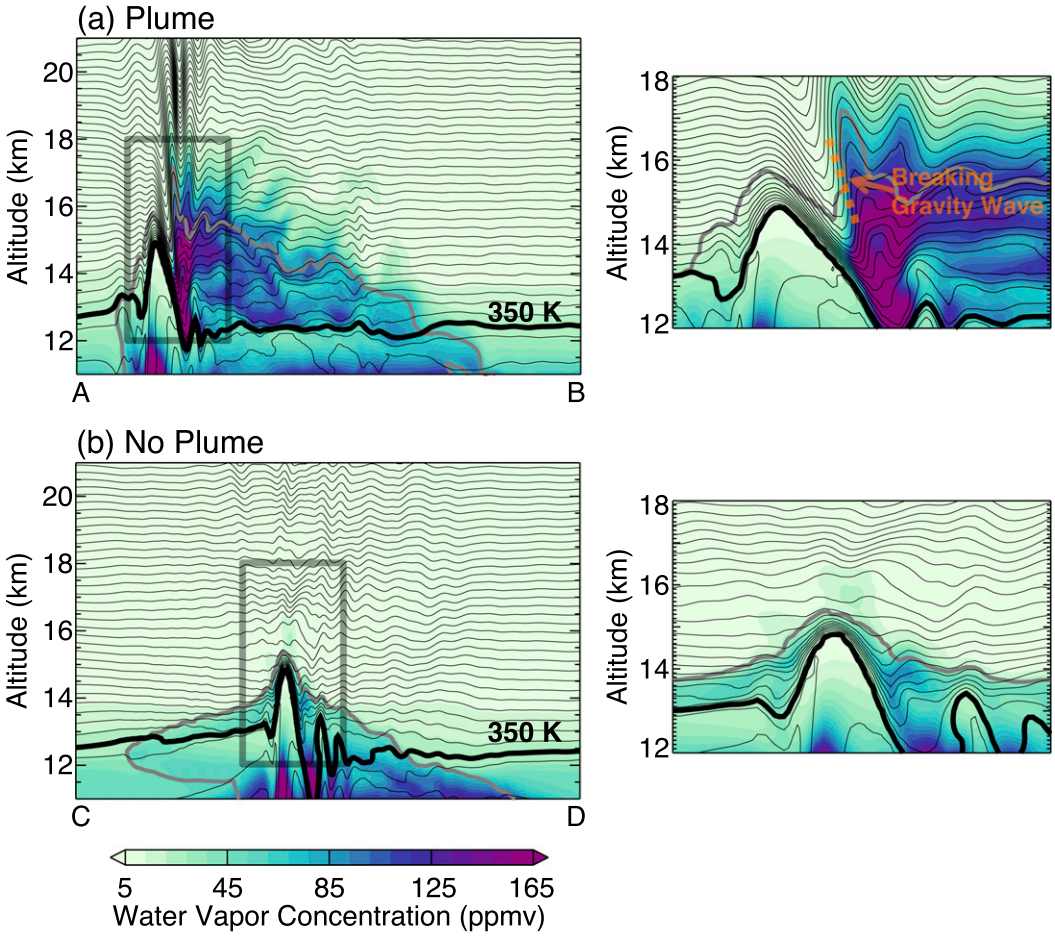

FIG. 10. (left) From idealized WRF simulations, vertical cross sections of water vapor concentration (ppmv; color fill), the cloud boundary (gray line; cloud particle mixing ratio $\geq 0.01\ \mathrm{g\,kg^{-1}}$), and potential temperature at 5-K intervals (black lines) for the simulation (a) with and (b) without an above-anvil cirrus plume. The thickest potential temperature contour in each section represents the altitude of the tropopause in this case (~350 K). (right) Zoomed-in views corresponding to the smaller regions of the cross sections identified by the thick dark gray transparent boxes in (left).

breaking and above-anvil cirrus enable a single convective storm to have a measurable, relatively large-scale impact on the composition of the lower stratosphere.

5. Summary and discussion

This study examined the mechanisms responsible for the formation and maintenance of above-anvil cirrus plumes in extratropical convection. We employed a diverse set of high-resolution observations or observation-based datasets to examine the environmental and physical characteristics of observed cases of convection with above-anvil cirrus plumes, including GOES visible and infrared imagery, WSR-88D volumes, and output from the ERA-Interim. It was found that all storms with above-anvil cirrus plumes are tropopause-penetrating, suggesting that these clouds reside in the lower stratosphere. Based on this result, we analyzed an additional population of tropopause-penetrating storms without above-anvil cirrus plumes in order to better identify unique physical and/or environmental characteristics associated with their formation and tested four primary hypotheses: 1) the stability of the stratosphere must be low (i.e., near tropospheric), 2) the storm-relative horizontal wind in the UTLS must be large such that frequent gravity wave breaking and/or rapid stretching of the overshooting top occurs, 3) the storm must frequently penetrate or remain above the tropopause for a long period of time to provide a near-continuous source of cloud particles, and 4) the stratosphere must be near saturation prior to tropopause-penetrating convection so that plumes are formed in situ rather than injected by the convective overshoot. Through multi-observational tests of these hypotheses, we demonstrated that storms with

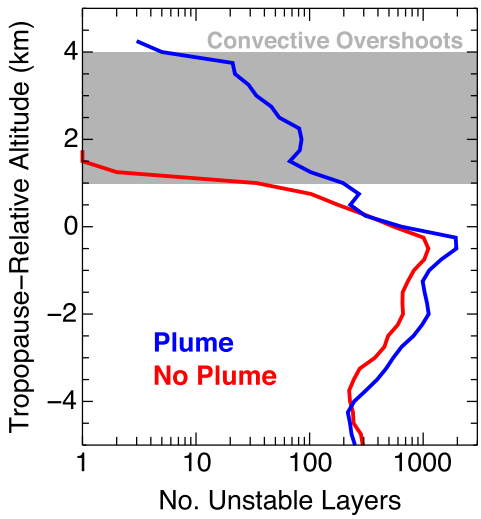

FIG. 11. From idealized WRF simulations, profiles of unstable-layer occurrences (negative vertical gradients of potential temperature) within cloud and at relative altitudes to the tropopause during the entire simulation period for the simulation with (blue) and without (red) above-anvil cirrus plumes. The gray color fill represents the layer of maximum cloud-top altitudes reached by the convective cores in each simulation.

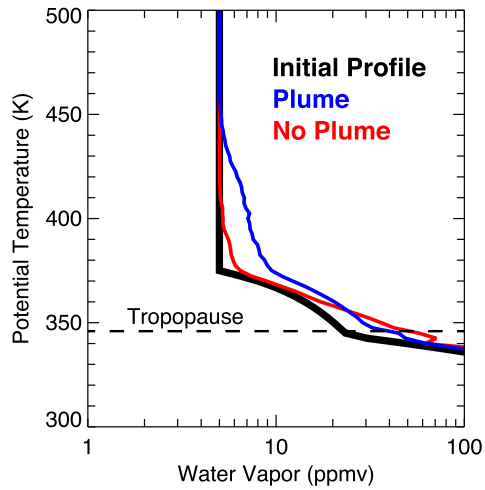

FIG. 12. From idealized WRF simulations, profiles of water vapor as a function of potential temperature at the final simulation time. The water vapor profile at initialization is given by the thick black line, the profile for the simulation without an above-anvil cirrus plume is the red line, and the profile for the simulation with an above-anvil cirrus plume is the blue line. The horizontal dashed black line represents the potential temperature of the tropopause in each simulation.

above-anvil cirrus plumes are associated with relatively large storm-relative UTLS winds. A weak relationship was found between above-anvil cirrus plume formation and the stability of the stratosphere (and overshooting depth), while no relationship was found with the duration of tropopause penetration or the humidity of the stratosphere.

Idealized WRF simulations with explicitly resolved convection reproduced the observed relationship between above-anvil cirrus plumes and storm-relative UTLS winds and were further examined to reveal the physical/dynamical mechanisms responsible for their formation and maintenance as well as their impact on stratospheric water vapor. The model simulations demonstrated that frequent gravity wave breaking was the primary mechanism responsible. In addition, despite similar tropopause penetration in each simulation, only the simulated storm with an above-anvil cirrus plume produced measurable enhancements in stratospheric water vapor. Furthermore, the gravity wave breaking and lofting of the above-anvil plume led to significant enhancements in water vapor, as much as a doubling of the initial concentration, up to altitudes of 18 km (6 km above the environmental tropopause) or potential temperatures of 440 K, well above the maximum altitudes achieved by the convective ascent alone (16 km). Additional recent modeling studies have also observed this behavior (e.g., Wang et al. 2016).

The results in this study have important broader implications for atmospheric transport [stratosphere–troposphere exchange (STE)] and numerical modeling studies. The strong support from the observational and modeling analyses here for the linkage between above-anvil cirrus plumes and injection of cloud particles into the stratosphere motivates future work on determining the scale and frequency of such features globally. For example, in many regions, ground-based remote sensing systems such as precipitation radars are either nonexistent or sparsely populated such that available information on the physical characteristics of convection is insufficient for identifying storms that are tropopause penetrating. Alternative satellite-based radars and lidars also suffer from poor spatial and/or temporal sampling. On the other hand, geostationary satellite imagery and corresponding detection of above-anvil cirrus plumes would enable analyses of STE from convection across the globe at appropriate spatial and temporal scales (including short-term climate change or climate variability). Development of reliable objective techniques to detect above-anvil cirrus in satellite imagery is a challenging and required step for the success of this approach. More extensive analyses using a combination of the radar data and satellite imagery employed in this study would also be worthwhile. Also, it is possible that additional factors not examined here, such as the microphysical composition of the convective cloud, are important to the formation and/or maintenance of above-anvil cirrus plumes. New in situ observations from aircraft would be beneficial for developing a deeper understanding of the characteristics of above-anvil cirrus plumes and their impact on the lower stratosphere.

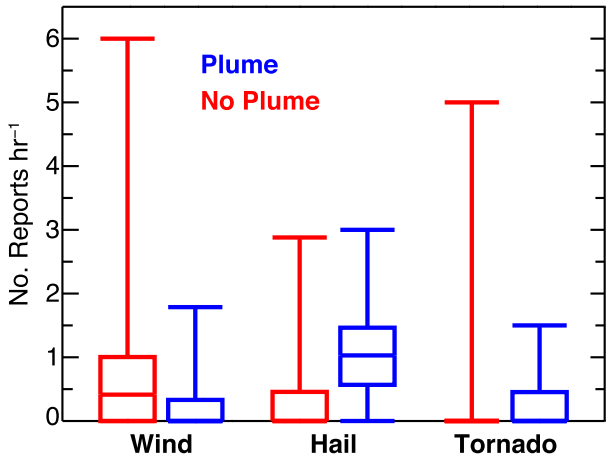

FIG. 13. Box-and-whisker plots (minima, lower quartile, median, upper quartile, and maxima) of storm reports (severe straight-line wind, severe hail, and tornado) from the NOAA SPC archive for storms with (blue) and without (red) above-anvil cirrus plumes. Units in each case are the number of reports per hour based on the trackable lifetime of each storm and reports considered are those within 20 km of a storm's location at the time the report is valid.

While gravity wave generation and breaking cannot be examined directly using the observational datasets available to this study, the offset in storm-relative winds between the two populations analyzed may enable identification of the characteristic gravity wave lengths generated in extratropical convection. A significant number of additional cases to that used here would be required to identify a robust transition (or threshold) for above-anvil cirrus formation, but such information would be valuable for future atmospheric dynamics and numerical modeling studies. In particular, given the known sensitivity between simulated convectively generated gravity wave spectra and model grid resolution, an observation-based gravity wave spectrum would help identify appropriate model designs for future numerical studies of convection and convective transport. Incorporating high-resolution balloon observations near in space and time to the observed storms for storm-relative wind analysis would also be worthwhile to assess potential errors from biases in the model analyzed winds used here.

Finally, though not a focus of this study, we thought it worthwhile to include a simple analysis here examining differences in severity between the two groups of tropopause-penetrating convection. Since the cases were first identified as days with a large number of severe weather reports in the NOAA SPC archive, we examined the frequency of severe reports per storm and scaled the storm report numbers by their radar-determined lifetime in an effort to normalize the populations. Figure 13 shows box-and-whisker plots of the resulting storm report frequencies for tornadoes, severe hail [exceeding 1 in. (2.54 cm) in diameter], and severe wind [that exceeding 50 kt (25.7 m s^{-1}) at ground level] for each population. Two things are worth noting here: 1) severe hail is the only report type that shows clear offsets in the storm report rate populations, with severe hail being more frequent in storms with above-anvil cirrus plumes, and 2) the remaining tornado and severe wind report-rate populations show smaller differences, with slightly higher tornado report rates in storms with above-anvil cirrus plumes and slightly higher severe wind report rates in storms without plumes. These differences between the two populations, especially that for hail, motivate future work on the severe weather problem. In particular, determining what physical/dynamical characteristics or possible limitations of the data lead to these differences is necessary for leveraging this information in forecasting and modeling applications.

Acknowledgments. We thank Ken Bowman at Texas A&M University and three anonymous reviewers for providing comments that helped improve the manuscript. We also thank Andrew Dzambo at the University of Oklahoma (now at University of Wisconsin–Madison) for help advising J. McAuliffe. J. McAuliffe was supported by the National Science Foundation (NSF) under Grant AGS-1062932, via a Research Experiences for Undergraduates (REU) program during summer 2015 in the National Weather Center at the University of Oklahoma. C. Homeyer was supported by NSF under Grant AGS-1522910 and the National Aeronautics and Space Administration (NASA) under Award NNX15AV81G. K. Bedka was also supported by NASA under Award NNX15AV81G.

REFERENCES

Adler, R. F., D. D. Fenn, and D. A. Moore, 1981: Spiral feature observed at top of rotating thunderstorm. *Mon. Wea. Rev.*, **109**, 1124–1129, doi:10.1175/1520-0493(1981)109<1124:SFOATO>2.0.CO;2.

——, M. J. Markus, D. D. Fenn, G. Szejwach, and W. E. Shenk, 1983: Thunderstorm top structure observed by aircraft overflights with an infrared radiometer. *J. Climate Appl. Meteor.*, **22**, 579–593, doi:10.1175/1520-0450(1983)022<0579:TTSOBA>2.0.CO;2.

——, ——, and ——, 1985: Detection of severe Midwest thunderstorms using geosynchronous satellite data. *Mon. Wea. Rev.*, **113**, 769–781, doi:10.1175/1520-0493(1985)113<0769:DOSMTU>2.0.CO;2.

Anderson, J. G., D. M. Wilmouth, J. B. Smith, and D. S. Sayres, 2012: UV dosage levels in summer: Increased risk of ozone loss from convectively injected water vapor. *Science*, **337**, 835–839, doi:10.1126/science.1222978.

Bedka, K. M., C. Wang, R. Rogers, L. D. Carey, W. Feltz, and J. Kanak, 2015: Examining deep convective cloud evolution using total lightning, WSR-88D, and GOES-14 super rapid

scan datasets. *Wea. Forecasting*, **30**, 571–590, doi:10.1175/WAF-D-14-00062.1.

Brunner, J. C., S. A. Ackerman, A. S. Bachmeier, and R. M. Rabin, 2007: A quantitative analysis of the enhanced-V feature in relation to severe weather. *Wea. Forecasting*, **22**, 853–872, doi:10.1175/WAF1022.1.

Crum, T. D., and R. L. Alberty, 1993: The WSR-88D and the WSR-88D operational support facility. *Bull. Amer. Meteor. Soc.*, **74**, 1669–1687, doi:10.1175/1520-0477(1993)074<1669:TWATWO>2.0.CO;2.

Dee, D. P., and Coauthors, 2011: The ERA-Interim reanalysis: Configuration and performance of the data assimilation system. *Quart. J. Roy. Meteor. Soc.*, **137**, 553–597, doi:10.1002/qj.828.

Del Genio, A. D., M.-S. Yao, and J. Jonas, 2007: Will moist convection be stronger in a warmer climate? *Geophys. Res. Lett.*, **34**, L16703, doi:10.1029/2007GL030525.

Dixon, M., and G. Wiener, 1993: TITAN: Thunderstorm Identification, Tracking, Analysis, and Nowcasting—A radar-based methodology. *J. Atmos. Oceanic Technol.*, **10**, 785–797, doi:10.1175/1520-0426(1993)010<0785:TTITAA>2.0.CO;2.

ECMWF, 2009: ERA-Interim project. National Center for Atmospheric Research Computational and Information Systems Laboratory Research Data Archive, accessed May 2015–May 2016, doi:10.5065/D6CR5RD9.

Forster, P. M. F., and K. P. Shine, 1999: Stratospheric water vapour changes as a possible contributor to observed stratospheric cooling. *Geophys. Res. Lett.*, **26**, 3309–3312, doi:10.1029/1999GL010487.

Fujita, T. T., 1982: Principle of stereoscopic height computations and their applications to stratospheric cirrus over severe thunderstorms. *J. Meteor. Soc. Japan*, **60**, 355–368.

Gettelman, A., P. Hoor, L. L. Pan, W. J. Randel, M. I. Hegglin, and T. Birner, 2011: The extratropical upper troposphere and lower stratosphere. *Rev. Geophys.*, **49**, RG3003, doi:10.1029/2011RG000355.

Han, L., S. Fu, L. Zhao, Y. Zheng, H. Wang, and Y. Lin, 2009: 3D convective storm identification, tracking, and forecasting—An enhanced TITAN algorithm. *J. Atmos. Oceanic Technol.*, **26**, 719–732, doi:10.1175/2008JTECHA1084.1.

Handwerker, J., 2002: Cell tracking with TRACE3D—A new algorithm. *Atmos. Res.*, **61**, 15–34, doi:10.1016/S0169-8095(01)00100-4.

Homeyer, C. R., 2014: Formation of the enhanced-V infrared cloud-top feature from high-resolution three-dimensional radar observations. *J. Atmos. Sci.*, **71**, 332–348, doi:10.1175/JAS-D-13-079.1.

——, and M. R. Kumjian, 2015: Microphysical characteristics of overshooting convection from polarimetric radar observations. *J. Atmos. Sci.*, **72**, 870–891, doi:10.1175/JAS-D-13-0388.1.

——, L. L. Pan, and M. C. Barth, 2014a: Transport from convective overshooting of the extratropical tropopause and the role of large-scale lower stratosphere stability. *J. Geophys. Res. Atmos.*, **119**, 2220–2240, doi:10.1002/2013JD020931.

——, and Coauthors, 2014b: Convective transport of water vapor into the lower stratosphere observed during double-tropopause events. *J. Geophys. Res. Atmos.*, **119**, 10 941–10 958, doi:10.1002/2014JD021485.

Iacono, M. J., J. S. Delamere, E. J. Mlawer, M. W. Shephard, S. A. Clough, and W. D. Collins, 2008: Radiative forcing by long-lived greenhouse gases: Calculations with the AER radiative transfer models. *J. Geophys. Res.*, **113**, D13103, doi:10.1029/2008JD009944.

Jiang, J. H., H. Su, C. Zhai, L. Wu, K. Minschwaner, A. M. Molod, and A. M. Tompkins, 2015: An assessment of upper troposphere and lower stratosphere water vapor in MERRA, MERRA2, and ECMWF reanalyses using Aura MLS observations. *J. Geophys. Res. Atmos.*, **120**, 11 468–11 485, doi:10.1002/2015JD023752.

Johnson, J. T., P. L. MacKeen, A. Witt, E. D. Mitchell, G. J. Stumpf, M. D. Eilts, and K. W. Thomas, 1998: The Storm Cell Identification and Tracking algorithm: An enhanced WSR-88D algorithm. *Wea. Forecasting*, **13**, 263–276, doi:10.1175/1520-0434(1998)013<0263:TSCIAT>2.0.CO;2.

Lacis, A. A., D. J. Wuebbles, and J. A. Logan, 1990: Radiative forcing of climate by changes in the vertical distribution of ozone. *J. Geophys. Res.*, **95**, 9971–9981, doi:10.1029/JD095iD07p09971.

Lane, T. P., and J. C. Knievel, 2005: Some effects of model resolution on simulated gravity waves generated by deep, mesoscale convection. *J. Atmos. Sci.*, **62**, 3408–3419, doi:10.1175/JAS3513.1.

——, and M. W. Moncrieff, 2008: Stratospheric gravity waves generated by multiscale tropical convection. *J. Atmos. Sci.*, **65**, 2598–2614, doi:10.1175/2007JAS2601.1.

——, R. D. Sharman, T. L. Clark, and H.-M. Hsu, 2003: An investigation of turbulence generation mechanisms above deep convection. *J. Atmos. Sci.*, **60**, 1297–1321, doi:10.1175/1520-0469(2003)60<1297:AIOTGM>2.0.CO;2.

Levizzani, V., and M. Setvák, 1996: Multispectral, high-resolution satellite observations of plumes on top of convective storms. *J. Atmos. Sci.*, **53**, 361–369, doi:10.1175/1520-0469(1996)053<0361:MHRSOO>2.0.CO;2.

Mack, R. A., A. F. Hasler, and R. F. Adler, 1983: Thunderstorm cloud top observations using satellite stereoscopy. *Mon. Wea. Rev.*, **111**, 1949–1964, doi:10.1175/1520-0493(1983)111<1949:TCTOUS>2.0.CO;2.

Mansell, E. R., C. L. Ziegler, and E. C. Bruning, 2010: Simulated electrification of a small thunderstorm with two-moment bulk microphysics. *J. Atmos. Sci.*, **67**, 171–194, doi:10.1175/2009JAS2965.1.

McCann, D. W., 1983: The enhanced-V: A satellite observable severe storm signature. *Mon. Wea. Rev.*, **111**, 887–894, doi:10.1175/1520-0493(1983)111<0887:TEVASO>2.0.CO;2.

Menzel, W. P., and J. F. W. Purdom, 1994: Introducing GOES-I: The first of a new generation of geostationary operational environmental satellites. *Bull. Amer. Meteor. Soc.*, **75**, 757–781, doi:10.1175/1520-0477(1994)075<0757:IGITFO>2.0.CO;2.

Negri, A. J., 1982: Cloud-top structure of tornadic storms on 10 April 1979 from rapid scan and stereo satellite observations. *Bull. Amer. Meteor. Soc.*, **63**, 1151–1159.

NOAA, 1994: NOAA Geostationary Operational Environmental Satellite Imager Data. NOAA Comprehensive Large Array-Data Stewardship System, accessed May 2015–May 2016. [Available online at https://www.class.ncdc.noaa.gov/saa/products/search?sub_id=0&datatype_family=GVAR_IMG&submit.x=9&submit.y=2.]

NOAA/NWS/ROC, 1991: NOAA Next Generation Radar (NEXRAD) Level II Base Data. NOAA National Centers for Environmental Information, accessed May 2015–May 2016, doi:10.7289/V5W9574V.

Romps, D. M., J. T. Seeley, D. Vollaro, and J. Molinari, 2014: Projected increase in lightning strikes in the United States due to global warming. *Science*, **346**, 851–854, doi:10.1126/science.1259100.

Rosenfeld, D., 1987: Objective method for analysis and tracking of convective cells as seen by radar. *J. Atmos. Oceanic Technol.*, **4**, 422–434, doi:10.1175/1520-0426(1987)004<0422:OMFAAT>2.0.CO;2.

Setvák, M., and C. A. Doswell, 1991: The AVHRR channel 3 cloud top reflectivity of convective storms. *Mon. Wea. Rev.*, **119**, 841–847, doi:10.1175/1520-0493(1991)119<0841:TACCTR>2.0.CO;2.

——, K. Bedka, D. T. Lindsey, A. Sokol, Z. Charvát, J. Šťástka, and P. K. Wang, 2013: A-Train observations of deep convective storm tops. *Atmos. Res.*, **123**, 229–248, doi:10.1016/j.atmosres.2012.06.020.

Skamarock, W. C., and Coauthors., 2008: A description of the Advanced Research WRF version 3. NCAR Tech. Note NCAR/TN-475+STR, 113 pp., doi:10.5065/D68S4MVH.

Solomon, D. L., K. P. Bowman, and C. R. Homeyer, 2016: Tropopause-penetrating convection from three-dimensional gridded NEXRAD data. *J. Appl. Meteor. Climatol.*, **55**, 465–478, doi:10.1175/JAMC-D-15-0190.1.

Solomon, S., K. H. Rosenlof, R. W. Portmann, J. S. Daniel, S. M. Davis, T. J. Sanford, and G.-K. Plattner, 2010: Contributions of stratospheric water vapor to decadal changes in the rate of global warming. *Science*, **327**, 1219–1223, doi:10.1126/science.1182488.

Spinhirne, J. D., M. Z. Hansen, and J. Simpson, 1983: The structure and phase of cloud tops as observed by polarization lidar. *J. Climate Appl. Meteor.*, **22**, 1319–1331, doi:10.1175/1520-0450(1983)022<1319:TSAPOC>2.0.CO;2.

Trapp, R. J., and K. A. Hoogewind, 2016: The realization of extreme tornadic storm events under future anthropogenic climate change. *J. Climate*, **29**, 5251–5265, doi:10.1175/JCLI-D-15-0623.1.

——, N. S. Diffenbaugh, H. E. Brooks, M. E. Baldwin, E. D. Robinson, and J. S. Pal, 2007: Changes in severe thunderstorm environment frequency during the 21st century caused by anthropogenically enhanced global radiative forcing. *Proc. Natl. Acad. Sci. USA*, **104**, 19 719–19 723, doi:10.1073/pnas.0705494104.

Wang, P. K., 2003: Moisture plumes above thunderstorm anvils and their contributions to cross-tropopause transport of water vapor in midlatitudes. *J. Geophys. Res.*, **108**, 4194, doi:10.1029/2002JD002581.

——, K.-Y. Cheng, M. Setvák, and C.-K. Wang, 2016: The origin of the gullwing-shaped cirrus above an Argentinian thunderstorm as seen in CALIPSO images. *J. Geophys. Res. Atmos.*, **121**, 3729–3738, doi:10.1002/2015JD024111.

Weisman, M. L., and J. B. Klemp, 1982: The dependence of numerically simulated convective storms on vertical wind shear and buoyancy. *Mon. Wea. Rev.*, **110**, 504–520, doi:10.1175/1520-0493(1982)110<0504:TDONSC>2.0.CO;2.

WMO, 1957: Meteorology—A three-dimensional science: Second session of the commission for aerology. *WMO Bull.*, **4**, 134–138.